Pergamon

Int. J. Solids Structures Vol. 34, No. 6, pp. 741–754, 1997

0020-7683/97 $17.00 + .00

PII: S0020-7683(96)00035-2

AN INTERFEROMETRIC AND FINITE ELEMENT INVESTIGATION OF INTERFACIAL CRACK TIP FIELDS: ROLE OF MODE-MIXITY ON 3-D STRESS VARIATIONS

JAYDEEP K. SINHA, HAREESH V. TIPPUR and LIMING XU
Department of Mechanical Engineering, Auburn University, Auburn, Alabama 36849, U.S.A.

(*Received* 17 *November* 1995; *in revised form* 9 *February* 1996)

Abstract—The elasto-optic effects are mapped as $(\sigma_x+\sigma_y)$ contours near interfacial cracks in polymer-metal bimaterials using Mach–Zehnder interferometry. The stress fields are investigated when the crack planes are subjected to dominant tensile stresses and pure shear stresses. The optical measurements are examined in conjunction with companion finite element simulations for estimating the regions of dominant three dimensional stress variations near cracks. Results suggest that in the domain $(x, y > 0)$ the size of the region of dominant three dimensional effects is significantly smaller for the case of pure shear (for both positive and negative shears) when compared to the tensile stress dominated case for oscillation index $\varepsilon > 0$. The optical data analyzed by incorporating these observations improve the accuracy of crack tip parameter estimation. Copyright © 1997 Elsevier Science Ltd.

INTRODUCTION

Analyzing full-field crack tip data for direct quantification of fracture parameters is quite common. For example, crack tip parameters are often extracted from optical data by interpreting interference measurements using 2-D asymptotic or K-dominant field descriptions. One of the issues that has drawn attention in recent years is related to 3-D deformations near interfacial cracks. This has particular relevance when field quantities are used along with 2-D solutions for parameter estimation as in the case of many experimental methods. Due to the material property mismatch along an interface, three dimensional effects may be significantly different near the crack tip when compared to the homogeneous counterparts. Further, since interfacial cracks inherently undergo mixed-mode deformations, understanding the interaction between mode-mixity and the size of three dimensional zone is important.

A number of investigations in the past have pointed out that three dimensional deformations dominate the near tip region in *homogeneous* materials. Folias (1975) discussed the effects of sheet thickness in the solution of a three dimensional mixed boundary value problems in elastostatics. He showed that in the interior of the plate only the stresses σ_x, σ_y, σ_z, τ_{xy} are singular of the order 1/2 and in the vicinity of the corner all the stresses are singular of order $((1/2)+2\nu)$, where ν is the Poisson's ratio. Yang and Freund (1985) observed finite lateral contractions near a through crack in a planar object. Rosakis and Ravi-Chandar (1986) used the method of caustics to conclude that the size of the 3-D deformation region scales with the plate thickness. Their experiments indicated that 3-D deformations dominate a region of approximately one half of the plate thickness. Nakamura and Parks (1988) numerically studied 3-D deformations near an elastic crack. Recently, Krishnaswamy *et al.* (1991) have showed the significance of the 3-D crack tip deformations in interpreting caustics in elastodynamic investigations. Extensive 3-D deformations are also observed when cracks undergo elastoplastic deformations. Using Moire methods and laser-speckle photography Chiang and Hareesh (1988) investigated 3-D crack tip behavior in ductile sheets. Their results suggested a 3-D zone of size 0.7–1.0 times the sheet thickness depending on the direction of measurement. Zehnder and Rosakis (1990) used caustics to assess 3-D effects near edge cracks in ductile three-point-bend specimens up to 0.6 times

the plate thickness. Hom and McMeeking (1990) analyzed near tip stress and deformation fields and they compared the results with plane stress solution. They found a double shear band ahead of the crack tip which created a 3-D zone extending several sheet thicknesses ahead of the crack. Narasimhan and Rosakis (1988) have performed numerical investigation to assess the 3-D effects near a crack front in a ductile three-point bend specimen.

Investigations on crack tip three dimensionality near *interfacial cracks*, however, are relatively new. Recently, Nakamura (1991) performed 3-D finite element computations to investigate stress fields near interface cracks for the special case of oscillation index $\varepsilon = 0$. He examined stresses very close to the crack front to determine the existence and the size of the so-called K-field. Barsoum and Chen (1991) numerically investigated the 3-D field near the an interface crack. They showed that the crack tip singularity at the free surface corner to depend on the Poisson's ratio. Lee and Rosakis (1993) numerically analyzed the extent of the near-tip 3-D zone in a tensile stress dominated bimaterial system. Their results indicate severe near-tip three dimensionality around most of the near tip region (up to half of the specimen thickness) and extend all along the interface of width equal to one half sheet thickness. Pidaparti and Pontula (1995) have found that the rubber materials have much larger 3-D zones compared to their linear counterparts. They observed that the size of the region of dominant 3-D effects increases with material mismatch up to 3–6 times the thickness.

These 3-D interfacial crack investigations reported thus far have been generally numerical in nature and experimental investigations are currently lacking. Further, the crack tip three dimensionality is addressed when cracks are subjected to predominantly tensile stresses. One of the prominent features of an interfacial crack, however, is that it inherently undergoes mixed-mode deformations and failure response depends on the sense of the local shear (see, Tvergaard and Hutchinson (1993), Xu and Tippur (1995)). Hence, interfacial failure characterization, static or dynamic, involves the determination of fracture toughness for a wide range of mode-mixities (for example, see Tippur and Xu (1995)). Hence, understanding the role of mode-mixity on interfacial crack tip three dimensionality is important for experimentally determining of fracture toughness–crack tip mixity relationships. This is particularly important for pointwise measurement techniques (such as strain gage measurements) in the near tip region. In this work, high resolution optical mapping and finite element analyses have been carried out for investigating the role of mode-mixities on interfacial crack tip three dimensionality in finite thickness samples. The optical measurements and finite element data corresponding to $(\sigma_x+\sigma_y)$ are compared for arriving at the estimates of the size and the region of dominant 3-D effects. Subsequently, optical data is analyzed by incorporating these observations to quantify crack tip parameters more accurately.

MACH–ZEHNDER INTERFEROMETRY (MZI)

In this section the working principle of a Mach–Zehnder interferometer is briefly discussed. MZI is a full-field, high resolution, real-time optical technique which provides interference patterns that represent contours of $(\sigma_x+\sigma_y)$ (thickness average values). The interferometer is shown schematically in Fig. 1. The light source is a He–Ne laser beam expanded and collimated to approximately 50 mm diameter. The interferometer consists of a reference optical path 1 and a test optical path 2 created using two beam splitters (BS1 and BS2) and two surface mirrors (M1, M2). The path lengths are nominally equal and the two beams are recombined after M2. The optics is aligned to get a uniform fringes on the image plane. A fracture specimen made of an optically isotropic transparent material is placed in the test path 2. The complex amplitude distributions, E_1 and E_2, corresponding to paths 1 and 2 when 50/50 beam splitters are used are,

$$E_1 = A_o\, e^{(ikl)}, \quad E_2 = A_o\, e^{(ik[l+\delta l+(n_o-1)B])} \tag{1}$$

where l represents the nominal geometric length of the two paths 1 and 2, δl represents a

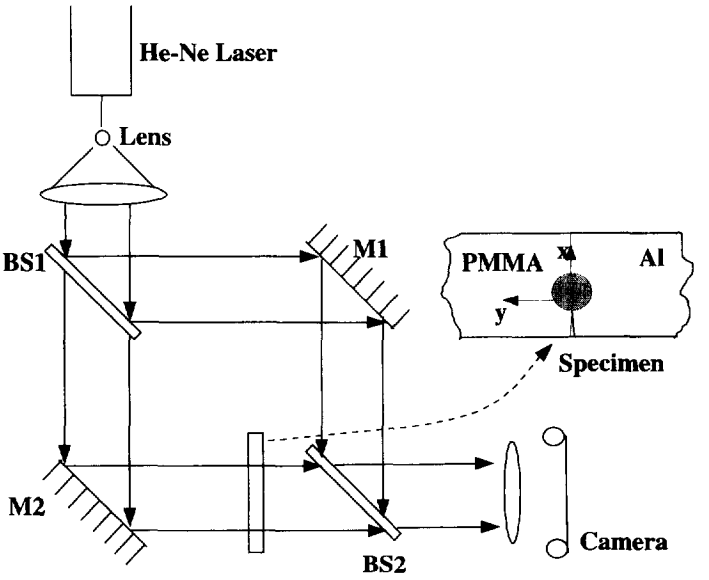

Fig. 1. Schematic of Mach–Zehnder interferometer.

constant difference in path lengths that may exist during the initial alignment, $k(=2\pi/\lambda)$ is the wave number, n_o and B are the nominal refractive index and the nominal thickness of the test specimen, respectively. Here, A_o is the constant amplitude for both reference and object waves. The term (n_o-1) corresponds to the optical path difference S between the two beams due to the specimen. The resultant spatial amplitude distribution on the image plane is given by, $E = E_1+E_2$. Then, the intensity distribution on the camera plane corresponding to the undeformed specimen is, $I = E\bar{E}$. Therefore,

$$I = 2A_o^2(1+\cos k[\delta l+(n_o-1)B]), \tag{2}$$

where $\bar{E}$ is the complex conjugate of E. For constructive interference on the image plane,

$$k[\delta l+(n_o-1)B] = 2N\pi$$
$$\text{or,}\quad \delta l+(n_o-l)B = N\lambda, \tag{3}$$

where N is the fringe order $(N = 0, \pm 1, \pm 2, \ldots)$. When the specimen undergoes deformation, E_2 becomes $E_2 = A_o e^{(ik[l+(n_o-1)B+\delta S])}$, where $\delta S(x,y)$ constitutes both $\delta B(x,y)$ (thickness change) and $\delta n_o(x,y)$ (refractive index change). Thus, the intensity distribution for the deformed specimen is given by,

$$I = 2A_o^2(1+\cos k[\delta l+(n_o-1)B+\delta S]). \tag{4}$$

Again, for constructive interference,

$$k[\delta l+(n_o-1)B+\delta S] = 2N'\pi$$
$$\delta S = (N'-N)\lambda+\mathcal{N}\lambda, \tag{5}$$

where $\mathcal{N} = (N'-N) = 0, \pm 1, \pm 2, \ldots$. From the above analysis it is clear that interference patterns represent contours of constant δS and the sensitivity of measurement is equal to λ per fringe. When loads are applied to the object, a combination of refractive index change (stress-optic effect) and thickness change (Poisson effect) constitute δS. The path difference can be related to the mechanical field using plane stress assumptions and mid-plane approximation (see Tippur *et al.* (1991)), as follows:

$$\delta S + cB(\sigma_x + \sigma_y), \tag{6}$$

c being the elasto-optic constant for the material. For PMMA $c = -0.92 \times 10^{-10}$ m^2/N.

INTERFACIAL CRACK TIP FIELDS

Specimen preparation

For this investigation, bimaterial specimens with a relatively large stiffness mismatch were made from model materials, namely, PMMA and aluminum. Two equal thickness ($B = 6$ mm) pieces were bonded along an edge using an adhesive consisting of methyl-methacrylate monomer (MMA) and a polymerizing agent at room temperature. The choice of the bond material provides a nominally bimaterial joint. The metallic surface was sand blasted prior to bonding to enhance bond strength. To avoid machining stresses, a chilled water mist was sprayed during the high speed machining (cutter speed 950 rpm; depth of cut 10 μm) of the PMMA half. A Teflon tape was inserted (25–50 μm thick) to produce a sharp edge discontinuity. Before testing, each specimen was optically examined in the MZI set-up under no-load condition to ensure that the interface was free from residual stresses.

Crack plane subjected to dominant tensile stress

First, crack tip stresses ($\sigma_x + \sigma_y$) were mapped using MZI for the case when the crack plane was subjected to dominant tensile stresses. A three-point-bend configuration, as shown in Fig. 2(a), was used for the purpose. The beam height (W) was 80 mm, the distance between the two supports (L) was 165 mm and crack length a was 25.4 mm ($a/W = 0.32$). In view of the experimental difficulty for applying the load exactly on the interface, the load was applied at a small distance 12.5 mm away from the interface. The corresponding interference patterns for an applied load of 335 N is shown in Fig. 2(b). Note that the interference patterns were seen only in the $y > 0$ region. Each fringe increment corresponds

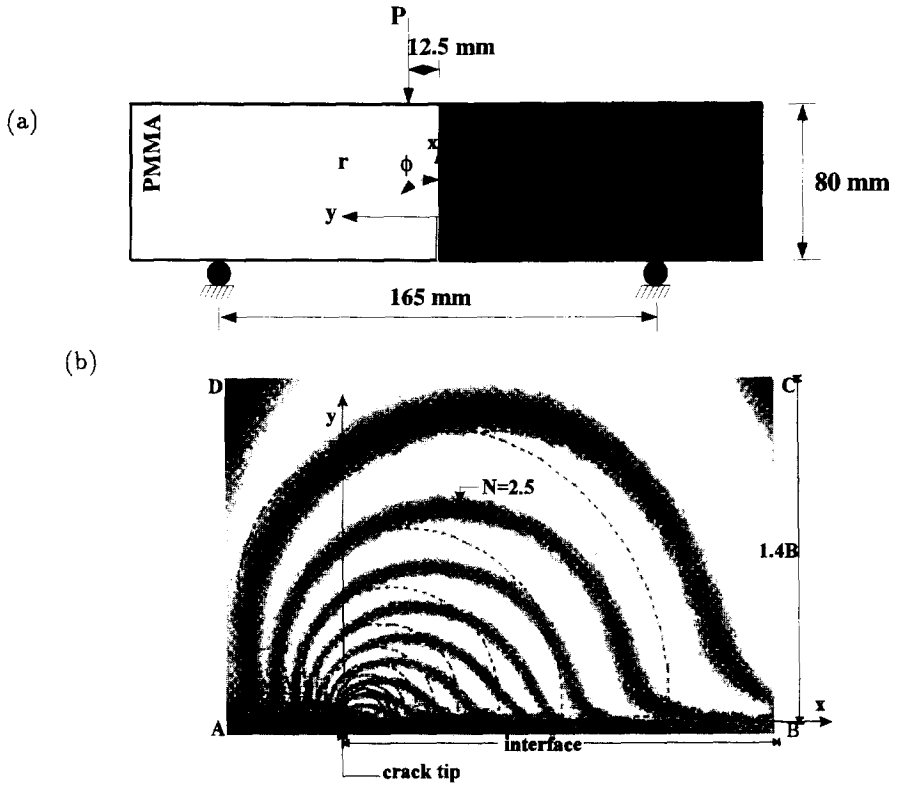

Fig. 2. (a) Bimaterial specimen and 3-point bending configuration; (b) MZI fringes (contours of $\sigma_x + \sigma_y$) around the interfacial crack tip. (1.1 MPa/fringe; optical path change of $\lambda/2$ produces one-half fringe.) Dotted lines from plane stress finite element simulation.

to an optical path length change of 633 nm or a change of 1.1 MPa. Excellent discernability of the interference fringes are evident even at small distances (<0.5 mm) away from the crack tip. The contours shown as dotted lines will be discussed later in this section.

To obtain an estimate of the size of the zone of dominant 3-D deformations near the crack tip, a complementary linear elastic, plane stress, finite element analysis was carried out using the ANSYS software package. The finite element model consisted of 2712 eight node plane stress quadrilateral elements and 8405 nodes (see Fig. 3a). The crack tip region was discretized using a fine mesh with 1056 crack tip elements within $0.55B$ radius and 1776 elements within $2B$ radius from the crack length. The inner most ring of elements were as small as $0.001a$, a being the crack length. The near tip mesh is shown in Fig. 3(b). No singularity element was used at the crack tip. The elements in the region $y > 0$ and $y < 0$ were assigned material properties of PMMA (material-1) and aluminum (material-2).

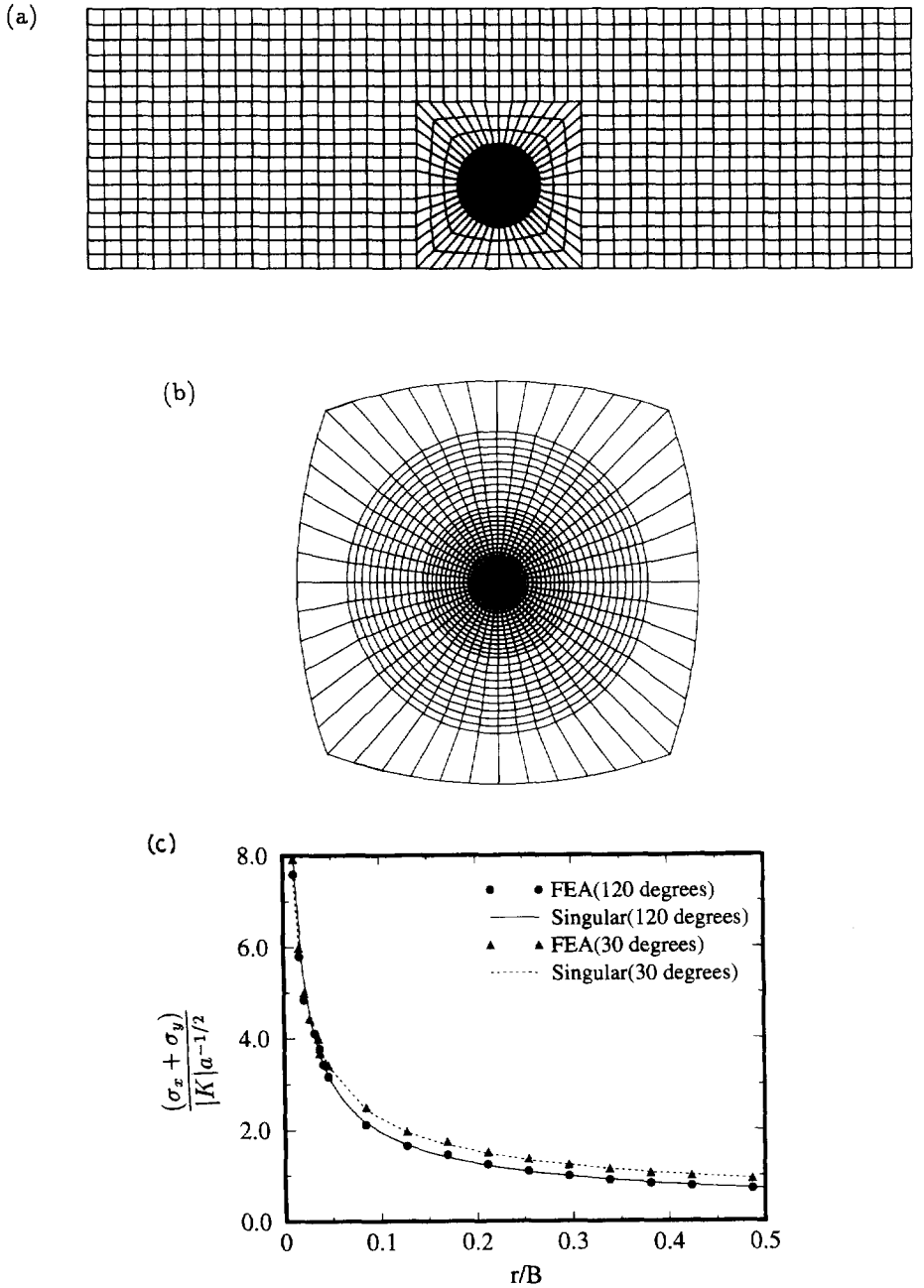

Fig. 3. (a) Finite element mesh; (b) near tip region, outer circle corresponds to $r/B = 2$, (c) comparison of stress fields between computations and singular descriptions.

The model was subjected to three-point bending as was done in the experiments. Non-dimensional $(\sigma_x+\sigma_y)$ from computations and singular field description are plotted as a function of (r/B) in Fig. 3(c) along two directions. The match between the two results is within 2% of each other. This demonstrates that the finite element discretization is fine enough to adequately capture the full-field singular behavior near the crack tip. Next, the $(\sigma_x+\sigma_y)$ contours with levels corresponding to the optical fringe orders were generated from the numerical results. A direct superposition of the experimental fringes and finite element contours around the crack tip is shown in Fig. 2(b) (broken lines) in the region $y > 0$. As can be seen, the match between the two results is good in certain regions around the crack tip while significant departures are observed close to the interface, ahead of and behind the crack tip. The agreement between the two results suggests that in those regions optical data adequately ($\pm 10\%$ error) represent the plane stress behavior. On the other hand, disagreement between the two suggests the potential influence of 3-D variations in the stress fields, not captured by the plane stress FE simulations in the immediate vicinity of the crack tip. The agreement between the two results is seen to be good in the region approximately $r/B > 0.3$ and $65° < \phi < 135°$, where (r, ϕ) represent the crack tip polar coordinates. In fact, the fringes and the numerical contours are in excellent agreement between 90–130° at much smaller radial distances. These observations are similar to the ones recently reported by Lee and Rosakis (1993) using finite element computations for a large stiffness mismatch bimaterial system. It should be noted that in case of mode-I crack in homogeneous materials (Rosakis and Ravi-Chandar (1986), Nakamura and Parks (1988)) the plane stress behavior is observed beyond $r/B \approx 0.5$ along the x-axis. On the contrary, the presence of the interface introduces three dimensional stress variations all along the interface and hence plane stress conditions are not established along the bond line. Next, these observations were quantified by defining error E_r as,

$$E_r = (\sigma_{\alpha\alpha}^{exp} - \sigma_{\alpha\alpha}^{FEA})/\sigma_{\alpha\alpha}^{exp}, \quad \alpha = x, y, \tag{7}$$

and $\sigma_{\alpha\alpha}^{exp}$ and $\sigma_{\alpha\alpha}^{FEA}$ correspond to experimental and finite element values of stresses at a generic point in the field (summation over α is implied). The optical data was gathered along discrete directions where sufficiently large number of fringe intersections occur with a radial line drawn from the crack tip. The corresponding numerical data was also generated from the finite element output. Since finite element nodes do not generally coincide with the fringe locations, the two sets of data were fitted with curves (of the form $\alpha_{\alpha\alpha}(r, \phi) = (\text{constant})r^{-\beta}$ where $\beta > 0$) and the fitted functions were used to calculate E_r at different $(r/B, \phi)$ values. In Fig. 4(a) E_r is plotted as a function of normalized distance r/B from the crack tip along discrete directions. As observed earlier, the error plot suggests that the data along 120° and 90° are within $\pm 10\%$ error band in the region beyond $r/B > 0.3$ while the error along 30° and 150° are in the range of 25–30%. Based on these observations in Fig. 4(b) a region of dominant three dimensional effects (unshaded region) is shown. The shaded region in Fig. 4(b), however, adequately represents plane stress behavior to within $\pm 10\%$ in $(x, y > 0)$. It should be emphasized that in the shaded region K-dominant assumptions may still not be valid and will be discussed later on.

Crack plane subjected to pure shear stress

The bimaterial specimens were loaded in asymmetric four-point-bending configuration to simulate pure shear conditions on the crack plane. The schematic of the specimen and the loading configuration is shown in Fig. 5(a). In this configuration, by simply varying the distance s between the interface and the loading axis different applied loading mixities can be realized. When $s = 0$, the crack plane is under pure shear. Since the crack tip deformations and the failure responses are distinctly different for the cases when the crack plane is subjected to 'negative' and 'positive' pure shears (see Xu and Tippur, 1995), experiments were conducted for both $+s$ and $-s$ arrangements. The schematic in Fig. 5(a) corresponds to the $-s$ configuration (net shear force on the crack plane is in the $-x$ direction). Other inplane dimensions for negative shear case were $C/W+1.03$ and $D/W+0.52$. Since the

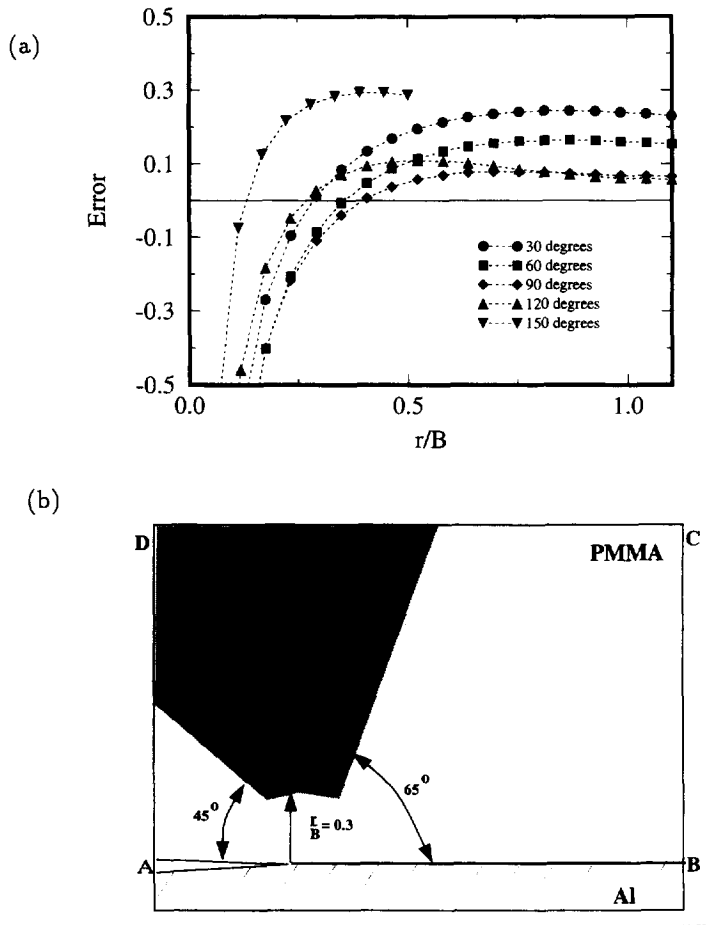

Fig. 4. (a) Deviation between optical measurements and FE computations along different radial directions for 3-point bend specimen, (b) regions of dominant three dimensional effects (unshaded region) and plane stress approximation (shaded region).

crack initiation typically occurred at a much smaller load with these parameters in the case of positive shear acting on the crack plane, the resulting number of fringes available for optical analysis in $y > 0$ were small. The reason for such a behavior is attributed to distinctly different crack tip deformations (opening and sliding) in these two situations. Crack tip nonlinearities further influence the failure process and are discussed in detail in Xu and Tippur (1995). This experimental difficulty was circumvented by changing the C/W and D/W ratios to 1.55 and 0.52, respectively. As can be seen from the following, the parameters C and D do not affect the applied stress mixity. The average shear and maximum normal stress acting on the plane are given by

$$\tau = \frac{P}{WB}\left(\frac{C-D}{C+D}\right), \quad \sigma = 6\tau\frac{s}{W}. \tag{8}$$

From the above, an applied load mixity at a point on the crack plane could be introduced as, say, $\Theta = \tan^{-1}(W/6s)$. Here, Θ is dependent on the eccentricity ration (s/W) and is independent of C and D.

The asymmetric four-point-bend samples were subjected to pure negative and positive shear loadings. The corresponding optical maps of $(\sigma_x + \sigma_y)$ were obtained in the crack tip vicinity and are shown in Fig. 5(b) and (c). As before, sensitivity of stress measurement is 1.1 MPa change between two successive (dark or light) fringes. Evidently, crack tip stress fields when pure shear is applied are quite pronounced behind the crack tip and relatively less spread-out ahead of the crack tip. Next, the previously described finite element model was subjected to asymmetric four-point-bend loading and the corresponding finite element

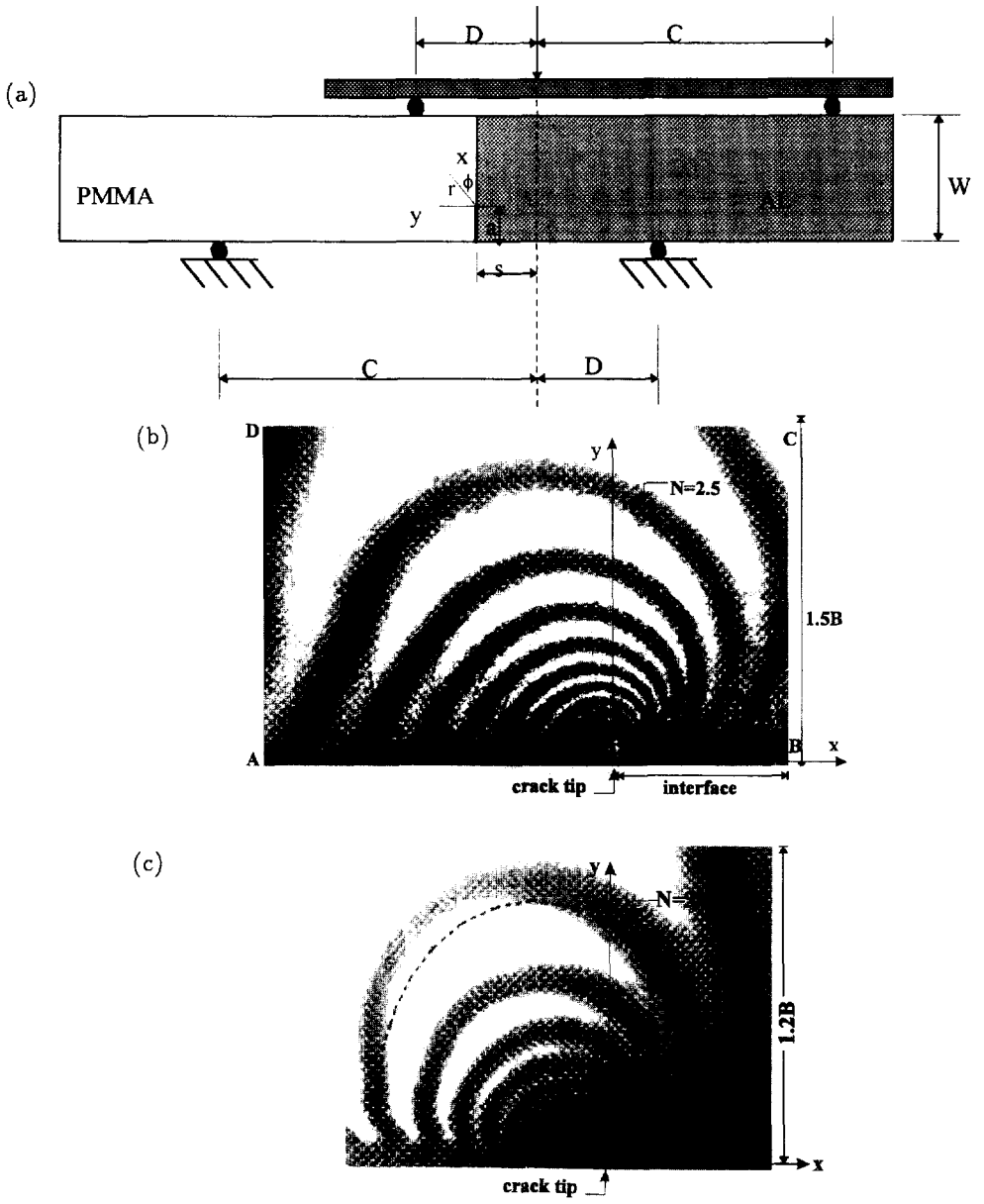

Fig. 5. (a) Bimaterial specimen and asymmetric 4-point bending configuration ('negative' shear set-up), (b), (c) MZI fringes (contours of $\sigma_x+\sigma_y$) around the interfacial crack tip for 'negative' and 'positive' shear acting on the interfacial plane. Dotted lines represent corresponding FE contours.

fringes representing contours of $(\sigma_x+\sigma_y)$ were synthesized from the numerical data. The two contour maps were superposed for negative and positive shear cases and are shown in Fig. 5(b), (c) (broken lines). As in the tensile stress dominated case, the agreement between the two results are excellent in certain regions while significant departures are evident in others. The agreement between the two results validates plane stress assumptions used in the computations while disagreement suggests zones where 3-D variations are significant. In both instances, in the region $r/B > 0.3$ and $30^\circ < \phi < 150^\circ$ good agreement between the experimental results and computations exist while the departures are significant elsewhere in $(x, y > 0)$. Once again, along the interface, 3-D effects are pronounced and hence a plane stress behavior has not taken hold in the neighborhood of the interface. These are further quantified in Fig. 6(a), (b) where the error E_r is plotted as a function r/B along discrete directions. Clearly, most of the radial directions outside $r/B > 0.3$ and $\phi = 30$–120° clearly fall within the $\pm 10\%$ error band. This suggests a much smaller zone of 3-D effects in the case of pure shear (positive or negative) acting on the crack plane in the $y > 0$ region.

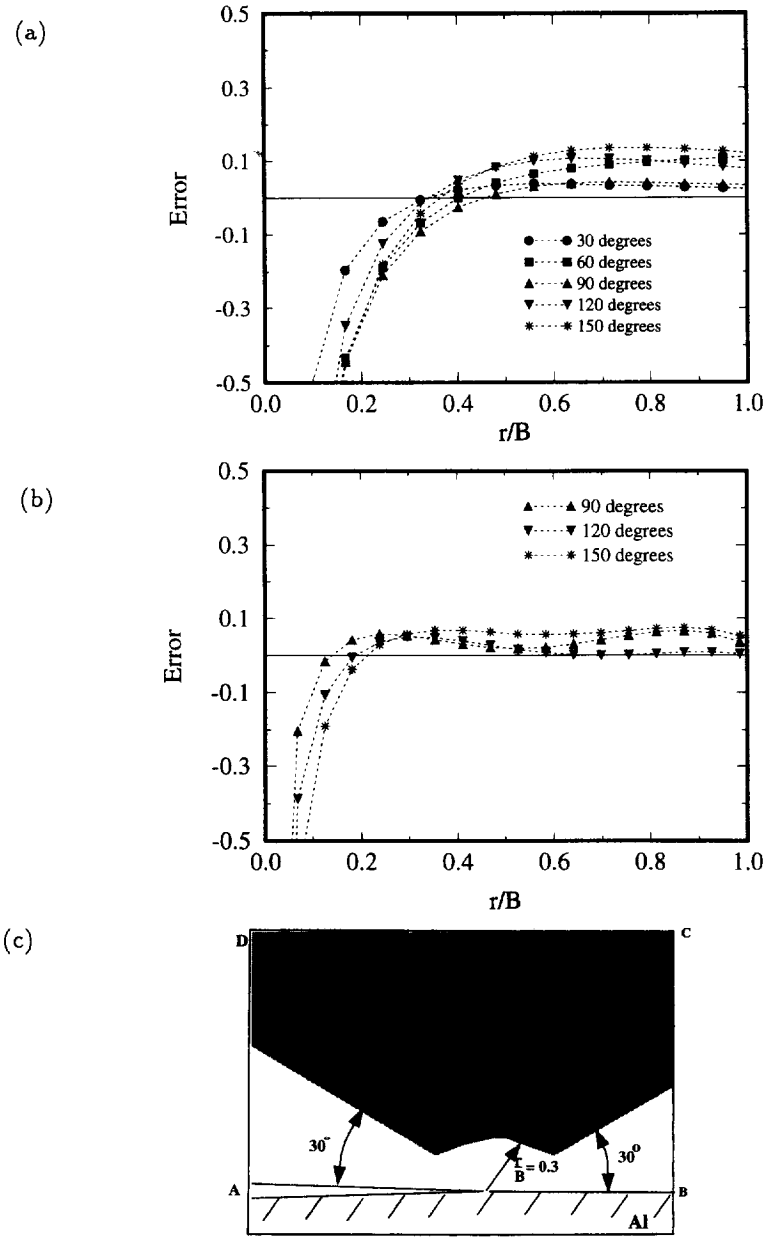

Fig. 6. (a), (b) Deviation between optical measurements and FE computations along different radial directions for 'negative' and 'positive' pure shear on the interface plane, (c) regions of dominant three dimensional effects (unshaded region) and plane stress approximation (shaded region).

When the sense of the shear is positive on the crack plane, the interference patterns were such that only limited data could be gathered ahead of the crack and hence the error plots are limited to fewer directions. Based on these observations, a schematic of the region of potential 3-D effects is shown Fig. 6(c) (unshaded region). As in Fig. 3(b), the shaded region corresponds to locations where plane stress assumptions are satisfactory.

From the above it becomes clear that the estimated region of dominant 3-D effects based on tensile stress dominated simulation is rather conservative. However, the accuracy of crack tip parameters estimation using least-squares approach typically improves when the data are gathered from a larger region near the crack tip. In view of this, the current results are encouraging as it suggests that one could gather data from a much larger region when the imposed shear component on the crack plane is increased.

An independent verification of the same has also been carried out using 3-D FE simulations of the above cases. The FE discretization used in these simulations was relatively

coarser than the 2-D simulations presented earlier due to limitations in the computer memory resources. However, we are only seeking a relative behavior of these cases and the results are supportive of the experimental observation. Finite element analyses were performed both in the tensile dominated and shear dominated cases for the same geometry of the specimen and loading conditions. Only one-half thickness of the specimen was modeled considering the symmetry of the problem about the midplane. Three layers of eight node (3 d.o.f./node) brick elements through the half thickness were used. The mesh was graded in the thickness direction such that the nodes are located on planes that are at $(z/B) = 0.0, 0.30, 0.45, 0.5$. It consisted of 5244 elements and 7308 nodes.

To quantify three dimensionality Rosakis and Ravi-Chandar (1986) have defined the so-called plane strain constraint $C_\varepsilon = \sigma_z/\nu(\sigma_x+\sigma_y)$ and is subsequently used in several other investigations. Under plane stress conditions this parameter is zero and is equal to ± 1 under plane strain conditions. Three dimensional stress analyses were performed separately for the tensile and shear dominated cases and the color plots of C_ε variations are shown in Fig. 7(a), (b). Note that these are not integrated effects as seen in the experiments but only information pertaining to the midplane. In Fig. 7(a) substantially larger regions of three

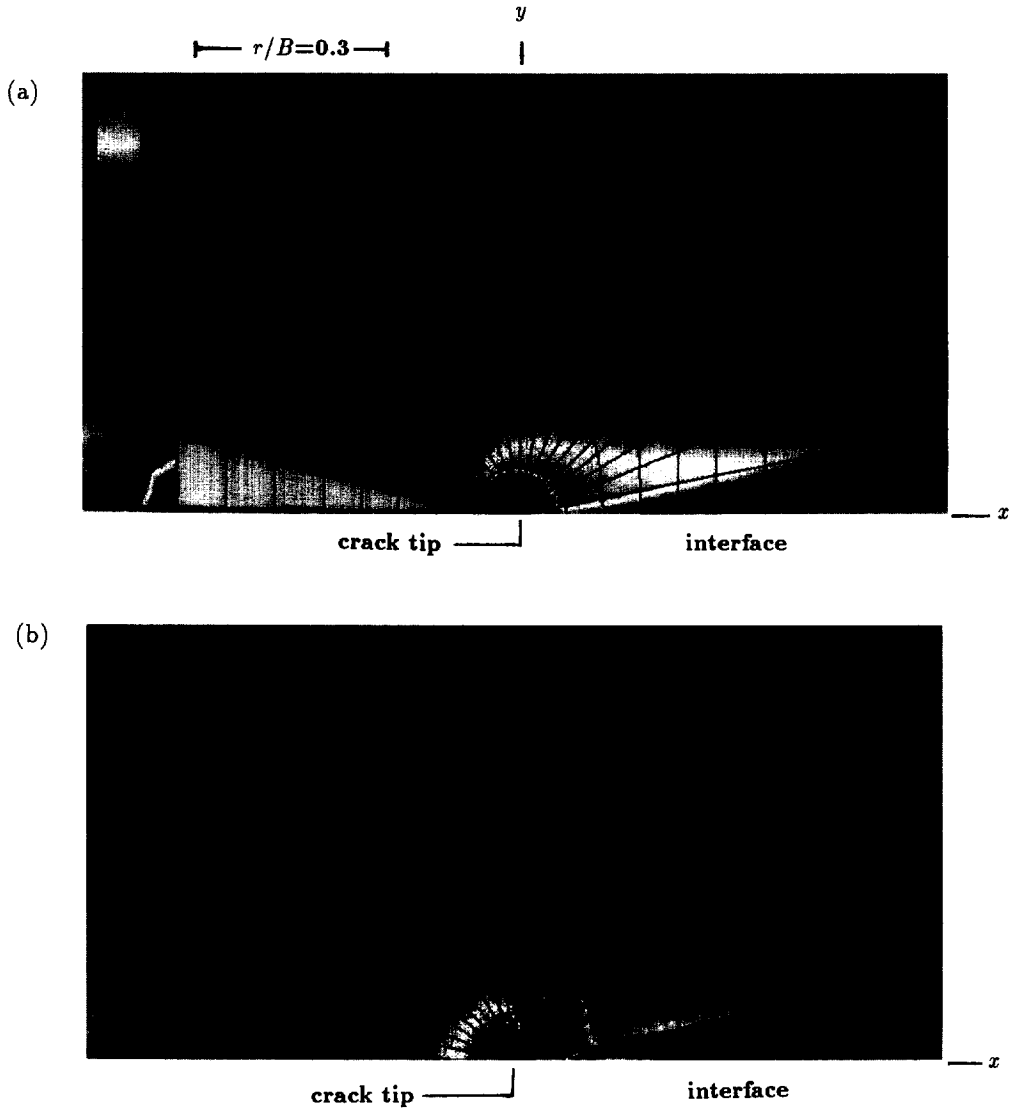

Fig. 7. Plot of plane strain constraint C_ε on the midplane in $y > 0$ region from 3-D FE computations. Interface subjected to (a) dominant tensile stress, (b) pure shear stress.

dimensional effects were observed in the region close to the crack tip and along the interface. (Note that the angular intervals between radial lines emanating from the crack tip are not equal.) In the region behind the crack tip there is clear evidence of a rather large value $C_\varepsilon(\approx -1)$ stretching along the crack flanks in a wedge. (The sudden change in C_ε from -1 to $+1$ (pink to red) over one element along the crack flank is an artifact of the post-processor and should be ignored.) Only in a wedge 65–135° and beyond $r/B = 0.3$ is the plane strain constraint relatively low ($< \pm 0.15$). These observations are consistent with the ones reported recently by Lee and Rosakis (1993) for a bimaterial sheet of thickness 4.5 mm. On the other hand, when we examine Fig. 7(b) in $y > 0$, plane constraint variations are quite different. A much larger region, say from 30–160° and beyond $r/B > 0.3$ show a relatively small value of C_ε when compared to Fig. 7(a). This seems to further support the experimental observations presented earlier. Of course, C_ε values are negligibly small for the layer adjacent to the surface and are not shown here.

Extraction of crack tip parameters from optical data

Having estimated a zone of prominent 3-D stress variations, next we proceed to extract interfacial crack tip parameters from the interference patterns by incorporating the above observations. Considering the material above the interface ($0 < \phi < \pi$), and following Rice (1988), the asymptotic expression for MZI fringes can be derived:

$$cB(\sigma_x+\sigma_y) = 4cB \sum_{n=1,3,5\ldots}^{\infty} e^{\varepsilon(\phi-\pi)} r^{[(n/2)-1]} \left\{ A_n \cos\left[\left(\frac{n}{2}-1\right)\phi - \varepsilon \ln\left(\frac{r}{a}\right)\right] + B_n \sin\left[\left(\frac{n}{2}-1\right)\phi - \varepsilon \ln\left(\frac{r}{a}\right)\right]\right\} + \frac{8cBc_2}{c_1+c_2} \sum_{n=2,4,6\ldots}^{\infty} r^{[(n/2)-1]} \left\{ A_n \cos\left(\frac{n}{2}-1\right)\phi + B_n \sin\left(\frac{n}{2}-1\right)\phi \right\} \tag{9}$$

$$= \mathcal{N}\lambda, \tag{10}$$

where $c_i = (\kappa_i+1)/\mu_i$, $\kappa_i = (3-\nu_i)/(1+\nu_i)$ for plane stress ($i = 1$ for PMMA and $= 2$ for aluminum) and $\mathcal{N} = 0, \pm 1, \pm 2\ldots$ denote fringe orders. A_n and B_n ($n = 1, 2, 3\ldots$) are the constant coefficients of the asymptotic expansion. Here μ and ν represent shear modulus and Poisson's ratio respectively, and

$$\varepsilon = \frac{1}{2\pi} \ln \frac{\mu_1 + \mu_2\kappa_1}{\mu_2 + \mu_1\kappa_2},$$

is the oscillation index. For the bimaterial under consideration $\varepsilon = 0.098$ for plane stress. Note that, the complex stress intensity factor is related to A_1 and B_1 as follows,

$$(Ka^{i\varepsilon}) = 2\sqrt{2\pi}\cosh(\pi\varepsilon)(A_1 + iB_1).$$

The phase of $(Ka^{i\varepsilon})$ $(= \tan^{-1} \mathrm{Im}(Ka^{i\varepsilon})/\mathrm{Re}(Ka^{i\varepsilon}))$ is the crack tip mode-mixity $\psi(a)$.

All fringe patterns in Figs 2 and 5 were digitized along discrete radial directions for obtaining the fringe location (r, ϕ) and the fringe order $(\mathcal{N})$ data. Only the data corresponding to the shaded region were used in the analysis. The fracture parameters were extracted using overdeterministic least-squares procedure. The so-called Q-R decomposition technique was used in the least-squares analysis for solving the resulting system of algebraic equations. In the past few investigations reported by the authors (Xu and Tippur (1995), Ganeshan (1994)), the advantages of Q-R decomposition over conventional methods has become evident and hence additional details on the method are included in Appendix A. Also, K-dominant assumptions (eqn (9)) were relaxed during the analysis

and higher order terms were incorporated in order to account for possible non-singular contributions to the field at distances beyond the anticipated 3-D zone.

The procedure consisted of minimizing the error function $\Phi(r, \phi; A_1, B_1, A_2, B_2, \ldots)$, $= \Sigma_{i=1}^{m} [F_i - F_i^{exp}]^2$, with respect to the constants of the series A_n and B_n ($n = 1, 2, 3, \ldots$). Here F and F^{exp} are the right hand sides in eqn (9), m denotes the total number of data points used in the analysis. The digitized data was first analyzed under the assumption of K-dominance ($n = 1$; unknown coefficients: A_1, B_1). For example, the difference between the optical data and the least-squares fit in Fig. 8(a) (for shear dominated case shown in Fig. 5(b)) suggests possible influence of non-singular stresses to the crack tip field in regions beyond the estimated 3-D zone and a need for including higher order terms in the least-squares analysis. However, details of higher order contributions such as the number of higher order terms (n) to be used in the analysis and the relative importance of each term compared to the others is unknown *a priori*. Therefore, higher order contributions were included sequentially until the match between the least-squares fit and the data was satisfactory and stable values of the mode-mixity were achieved (see Table A1). The result for the case when $n = 3$ in eqn (9) (unknown coefficients A_1, B_1, A_2, A_3, B_3) is shown in Fig. 8(b). A good agreement between the least-squares fit and measured data is clearly evident when higher order terms are incorporated into the analysis. The crack tip parameters obtained from the above analysis for all the cases considered in this paper are compiled in Table 1. The table also includes FE counterparts of the same obtained using J-integral calculations and a subsequent mode partitioning using interaction integral method proposed by Shih and Asaro (1988) and codes developed in Xu and Tippur (1995). Good agreement

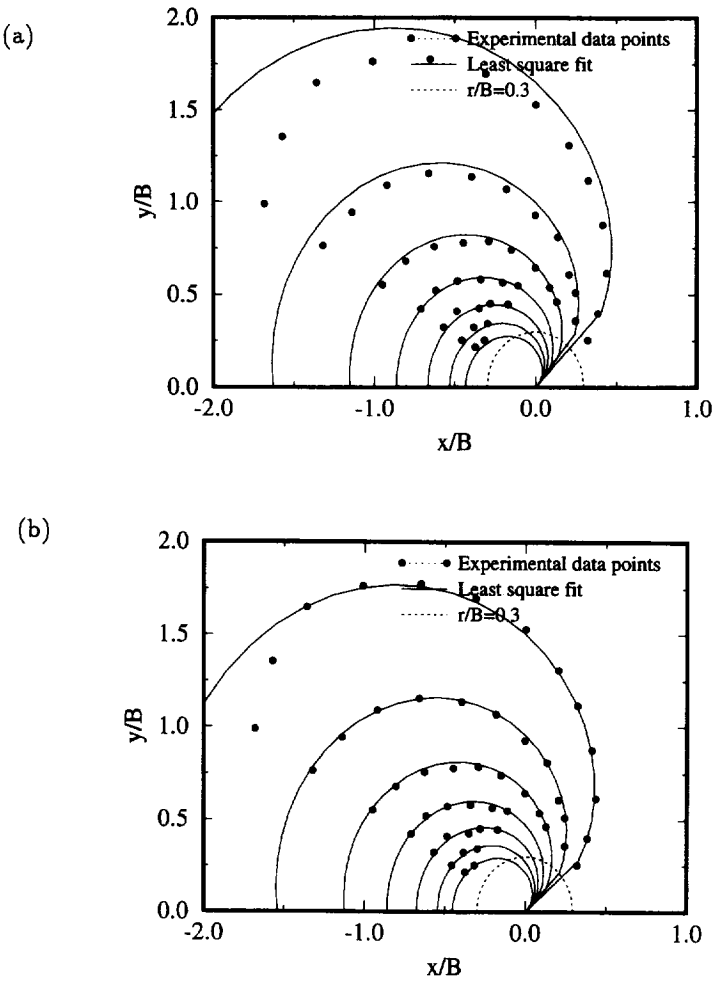

Fig. 8. Least-squares analysis of optical data for the case of 'negative' shear loading on the interface plane; (a) with only K-dominant terms, (b) with asymptotic expansion with five constant coefficients.

Table 1.

Loading	Experimental (data from shaded region) $\mathrm{Re}(Ka^{i\varepsilon})^{exp}$	Experimental (data from shaded region) $\mathrm{Im}(Ka^{i\varepsilon})^{exp}$	Plane stress FEA $\mathrm{Re}(Ka^{i\varepsilon})^{exp}$	Plane stress FEA $\mathrm{Im}(Ka^{i\varepsilon})^{exp}$	Experimental (data from shaded + unshaded regions) $\mathrm{Re}(Ka^{i\varepsilon})^{exp}$	Experimental (data from shaded + unshaded regions) $\mathrm{Im}(Ka^{i\varepsilon})^{exp}$
Pure shear (+)	−0.08	0.42	−0.10	0.38	−0.47	0.58
Pure shear (−)	0.30	−0.71	0.29	−0.69	0.39	−1.0
Tensile	0.58	0.13	0.56	0.06	0.77	0.13

between the optical measurements using the data in the shaded region for least-squares analysis (column 1) and finite element computations (column 2) are clearly evident. Further, the stress intensity factor results for these cases when all the digitized data points in both shaded and unshaded regions were used in the least-squares analysis (without taking into account potential 3-D stress variations) is also shown (column 3). The results in column 3 show poor correlation with the finite element computations. It should be emphasized that least-squares analyses of optical data are generally robust and do not show susceptibility to minor errors at individual data points. However, such an advantage does not exist when dealing with pointwise data in the field and 3-D effects such as the ones reported here could directly affect the error of the estimated parameter.

CONCLUSIONS

A complementary optical-finite investigation of an interface crack in a large elastic mismatch bimaterial system suggests that mode-mixity affects the size of the region of three dimensional effects. The extreme cases of applied load mixities, namely, predominantly tensile stress and pure shear stress (positive and negative), acting on the crack plane, suggest that there is a significant reduction in the size of the region of 3-D effects in the latter when compared to the former in $y > 0$ for $\varepsilon > 0$. That is, estimated zones of dominant 3-D effects based on former tend to be conservative for general situations of mixities for an interfacial crack. This is encouraging from the view point of experimental evaluation of fracture parameters using near tip measurements wherein data gathered from a larger region near the crack tip often improves the accuracy of parameter estimation. The regions where plane stress assumptions are adequate have been identified. By incorporating the experimental observations into the optical data analysis, fracture parameters have been accurately measured. Importance of avoiding data from the regions of dominant 3-D stress variations in experimental evaluation of crack tip parameters is demonstrated. Lastly, Mach–Zehnder interferometry is shown to be a potential tool in interfacial fracture investigations.

Acknowledgement—The research is supported by NSF Grant CMS-9313153.

REFERENCES

Barsoum, R. S. and Chen, T. (1991). Three-dimensional surface singularity of an interface crack. *Int. J. Fract.* **50,** 221–237.

Chiang, F. P. and Hareesh, T. V. (1988). Three-dimensional crack tip deformations: an experimental study and comparison to HRR field. *Int. J. Fract.* **36,** 243–257.

Folias, E. S. (1975). On the three-dimensional theory of cracked plates. *J. Appl. Mech.* **42,** 663–674.

Ganeshan, P. (1994). An interferometric study of interface fracture in bimaterials subject to thermo-mechanical loading. M.S. Thesis, Auburn University.

Hom, C. L. and McMeeking M. R. (1990). Large crack tip opening in thin elastic-plastic sheets. *Int. J. Fract.* **45,** 103–122.

Krishnaswamy, S., Rosakis, A. J. and Ravichandran, G. (1991). On the extent of dominance of asymptotic elastodynamic crack-tip fields: part II—numerical investigation of three-dimensional and transient effects. *J. Appl. Mech.* **58,** 95–103.

Kockler, N. (1994). *Numerical Methods and Scientific Computing*, Clarendon Press, Oxford.

Lee, Y. J. and Rosakis, A. J. (1993). Interfacial crack in plates: a three-dimensional numerical investigation. *Int. J. Solids Struct.* **30,** 3139–3158.

Nakamura, T. and Parks, D. M. (1988). Three-dimensional stress field near the crack front of a thin elastic plate. *J. Appl. Mech.* **55,** 805–813.

Nakamura, T. (1991). Three-dimensional stress fields of elastic interface cracks. *J. Appl. Mech.* **58,** 939–946.
Narsimhan, R. and Rosakis, A. J. (1990). Three-dimensional effects near a crack tip in a ductile three-point-bend specimen: numerical analysis. *J. Appl. Mech.* **57,** 607–617.
O'Dowd, N. P. Shih, C. F. and Stout, M. G. (1992). Test geometries for measuring interfacial fracture toughness. *Int. J. Solids Struct.* **29,** 571–589.
Pidaparti, R. M. V. and Pontula, G. (1995). Three-dimensional analysis of interface cracks in rubber materials. *Int. J. Fract.* **68,** 315–332.
Rice, J. R. (1988). Elastic fracture mechanics concepts for interfacial cracks. *J. Appl. Mech.* **55,** 98–103.
Rosakis, A. J. and Ravi-Chandar, K. (1986). On crack-tip stress state: an experimental evaluation of three-dimensional effects. *Int. J. Solids Struct.* **22,** 121–134.
Shih, C. F. and Asaro, R. J. (1988). Elastic-plastic analysis of cracks on bimaterial interfaces: part-I small scale yielding. *J. Appl. Mech.* **55,** 299–316.
Tippur, H. V. and Xu, L. (1995). Interfacial crack initiation under quasi-static and dynamic loading conditions: an experimental study. *Fatigue Fract. Engng Mater. Struct.* (in press).
Tvergaard, V. and Hutchinson, J. W. (1993). Influence of plasticity on mixed-mode interface toughness. *J. Mech. Phys. Solids* **41,** 1119–1135.
Yang, W. and Freund, L. B. (1985). Transverse shear effects for through-cracks in an elastic plate. *Int. J. Solids Struct.* **21,** 977–994.
Zehnder, A. T. and Rosakis, A. J. (1990). Three-dimensional effects near a crack tip in a ductile three-point bend specimen—an experimental investigation using interferometry and caustics. *J. Appl. Mech.* **57,** 618–626.
Xu, L. and Tippur, H. V. (1995). Fracture parameters for interfacial cracks: an experimental-finite element study of crack tip fields and crack initiation toughness. *Int. J. Fract.* **71,** 345–363.

APPENDIX A

The minimization of least-squares error during the optical data analysis using asymptotic interface crack tip fields results in a system of linear algebraic equations of the form $[\mathscr{A}]\{\mathscr{X}\} = \{\mathscr{R}\}$ where $[\mathscr{A}]$ is a square matric and $\{\mathscr{R}\}$, $\{\mathscr{X}\}$ are vectors of size equal to the number of coefficients in the expansion. It should be emphasized that when more number of terms in the expansion (eqn (9)) are considered in the analysis, matrix $[\mathscr{A}]$ often tends to be ill-conditioned as a result of the asymptotic nature of the fitting function. Traditional methods, say the L-U decomposition method, used for solving such a linear system of equations often lead to unstable results in this case. Therefore, in this investigation the so-called Q-R decomposition procedure was used in solving a system of equations in view of its stability characteristics and minimal computational errors. The reason behind this are that the algorithm involves operation on the data matrix directly, rather than the corresponding covariance matrix and involves only orthogonal rotations, which are numerically well conditioned (see Kockler (1994)). The direct evidence of efficacy of Q-R decomposition becomes evident by examining Table A1 where optical data corresponding to one of the cases considered in this investigation is shown. Convergence of the crack tip parameters when the number of terms in the asymptotic expansion are increased is clearly evident with Q-R decomposition technique while the L-U decomposition leads to unstable results, particularly regarding mode-mixity.

Table A1.

	Q-R decomposition			L-U decomposition		
Loading	No. of unknown coefficients	$\lvert(Ka^{ie})\rvert$ MPa$\sqrt{\text{m}}$	$\psi(a)$	No. of unknown coefficients	$\lvert(Ka^{ie})\rvert$ MPa$\sqrt{\text{m}}$	$\psi(a)$
Negative shear	2	0.50	−82.0°	2	0.44	−79.9°
	3	0.79	−65.9°	3	0.74	−65.6°
	5	0.77	−66.3°	5	0.70	−81.3°
	7	0.77	−66.3°	7	0.68	−109.0°